Transferrin-mediated targeting of bacteriophage HK97 nanoparticles into tumor cells

Rick K Huang[*,1,2], **Nicole F Steinmetz**[*,1,3,4], **Chi-Yu Fu**[3], **Marianne Manchester**[3], and **John E Johnson**[1,2,†]

[1] Department of Molecular Biology & Center for Integrative Molecular Biology, The Scripps Research Institute, 10550 North Torrey Pines Road, La Jolla, CA 92037, USA

[2] Department of Chemistry & Biochemistry, University of California, San Diego, 9500 Gilman Drive, La Jolla, CA 92093, USA

[3] Skaggs School of Pharmacy & Pharmaceutical Sciences, University of California, San Diego, 9500 Gilman Drive, MC 0657, La Jolla, CA 92093-0657, USA

[4] Department of Biomedical Engineering, Case Western Reserve University, 11100 Euclid Avenue, Cleveland, OH 44106, USA

Abstract

Aims—Next-generation targeted nanodevices are currently under development for imaging and therapeutic applications. We engineered HK97 viral nanoparticles (VNPs) for tumor cell-specific targeting.

Methods—A combination of genetic and chemical engineering methods were developed and applied to generate dual-labeled HK97 cysteine mutant particles displaying transferrin and fluorescent labels. The targeting properties of transferrin-conjugated VNPs were evaluated by *in vitro* experiments using different cancer cell lines.

Results—We found that HK97–tranferrin formulations were indeed targeted to cancer cells *in vitro* via the transferrin receptor. These studies highlight the utility and facilitate the further development of HK97-based VNPs.

Keywords

cancer; HK97; protein conjugation; targeted cellular entry; transferrin; viral nanoparticles

---

The development of imaging modalities and therapeutics with the ability to specifically target diseased cells and tissues is an important goal in next-generation biomedicine. Nanotechnology, in combination with tumor marker and ligand identification, has opened the door for the design of targeted formulations[1,2]. Nanomaterials such as quantum dots

---

(QDs), dendrimers, polymer vesicles, liposomes, and protein-based nano-structures such as viral nanoparticles (VNPs) are currently under investigation for such development [3–6]. VNPs are particularly attractive building blocks for several reasons as they are on the nanometer-size scale, monodisperse, polyvalent with a high degree of symmetry, biocompatible and biodegradable. Most importantly, new functionalities can be precisely tailored to VNPs by genetic modification or chemical bioconjugation. A particular advantage of VNPs, compared with synthetic nanomaterials such as liposomes, QDs or polymeric nanoparticles, is that VNPs are monodisperse structures that can be modified with atomic precision. Furthermore, one of the functions of the capsid is the protection of the encapsidated nucleic acids. The particles are thus extremely stable naturally, therefore allowing a range of chemistries to be applied. The high stability also facilitates structural integrity in plasma and even under gastric conditions for potential oral administration[7].

A variety of VNP platforms have been studied and developed to establish the importance of properties such as particle size, structural stability, surface charge, availability of addressable surface residues, interactions with mammalian cells and toxicity [4,8]. Gene-delivery applications utilizing mammalian viruses, such as adenovirus, adeno-associated virus and lentiviruses, have long been exploited [9–11]; however, a major concern with these human pathogens is the risk of induction of substantial toxic side effects even when using replication-deficient variants. More recently, the focus has shifted toward the utilization of VNPs derived from nonpathogenic plant viruses and bacteriophages [12–15]. These platforms are less likely to interact with the mammalian system and induce adverse effects (reviewed in [4]). Indeed, an animal study showed that intravenous administration of the plant VNP *Cowpea mosaic virus* (CPMV) did not induce any apparent toxic side effects in doses of up to 100 mg/kg body weight [16].

This study evaluated bacteriophage Hong Kong 97 (HK97) as a platform for the development of a specifically targeted VNP. HK97 is a λ-like phage that infects *Escherichia coli*. A member of the *Siphoviridae* family, HK97 is composed of a double-stranded, DNA-filled, 66-nm, nonenveloped capsid (head) and a long noncontractile tail with accessory proteins [17]. The wild-type virus head is composed of 415 copies of the capsid protein (gp5) arranged in pseudo T = 7 laevo icosahedral symmetry and a dodecameric portal complex, occupied in one of the fivefold symmetry vertices, associated with DNA packaging and tail attachment. The mature head is formed by a complex series of maturation transitions involving proteolytic cleavage and conformational changes [18,19]. During this process, the procapsid (P-II) undergoes a dramatic expansion from 56 to 66 nm, to form the mature capsid called head II (H-II). H-II subunits covalently cross-link to form catenated rings, resulting in a molecular chain-mail (Supplementary Figure 1 see online www.futuremedicine.com/doi/suppl/10.2217/nnm.10.99) and yielding one of the most robust VNPs characterized [20]. Particles can also be trapped in different maturation stages *in vitro* to generate P-I, P-II, expansion intermediates (EI), such as EI-I/II, and balloons described in Supplementary Figure 1. This collection of HK97 particles with different sizes, stabilities, and dynamics are versatile platforms for engineering multi-functional nanoparticles.

The potential advantages of HK97 VNPs are the precise control of maturation, structural stability, and relatively large size. Unlike most of the approximately 30-nm-sized VNPs such as *Cowpea chlorotic mottle virus* (CCMV) or *Red clover necrotic mottle virus* (RCNMV) that are currently under investigation for encapsidating therapeutics or materials [21,22], the 56-nm P-II or 66-nm H-II each offer a spacious interior with the potential to encapsidate a larger number of bioactive materials, such as therapeutic or imaging molecules. The internal capacity of HK97 P-II is 3.5×10^7 Å^3, (i.e., 900% larger than CCMV [3.48×10^6 Å^3] and approximately 690% larger than CPMV [4.39×10^6 Å^3] or

RCNMV [4.45×10^6 Å^3]). In addition, the T = 7 laevo HK97 provides more surface sites per particle for chemical modification, compared with T = 3 VNPs.

Maturation intermediates of HK97 were expressed at high yields in *E. coli* and prior biochemical and the structural characterization of HK97 allowed the design of mutants suitable for chemical attachment. Noninfectious virus-like particles (VLPs) of HK97, which do not contain the viral genome, were produced by coexpression of the capsid protein (gp5) and the virally encoded protease (gp4), which is required for head maturation to digest residues 2–103 of gp5 [23,24]. Prohead II (P-II) particles were produced and purified by previously described methods as were mature H-II particles [18,19].

Materials & methods

Cloning

C164 and C385 mutant particles were made from a wild-type P-II plasmid containing the genes encoding gp4 and gp5. The cysteines were introduced by replacing Ala164 (A164C) and Ser385 (S385C), of the gp5 protein, respectively. Mutagenesis was performed using standard quick change PCR in a Perkin Elmer thermocycler (Waltham, MA, USA) with primers C164: TGTTTACCAATAACGCCGACGTGGTGTGTGAGAAAGCACTGAAGCCAGAATCGGA and C385: CATCAAGGGCACCTTCTCTTCTGGCTGTTGATGGAGGGGGCGGGGAAA and their corresponding reverse complements synthesized by Integrated DNA Technologies (San Diego, CA, USA). DNA sequencing of the resulting plasmid constructs was performed by Eton Biosciences (San Diego, CA, USA).

Particle preparation

C164 and C385 P-II were expressed in BL21 (DE3) pLys cells carrying pT7-Hd2.9:4-vector. A total of 1 l of LB medium containing ampicillin 0.50 μg/ml and chloramphenicol 0.25 μg/ml was inoculated with an overnight culture, and when an optical density of 0.35–30.45 was reached (measured at a wavelength of 550 nm) the culture was induced at 28°C overnight with IPTG 0.4 mM. Cells were collected by centrifugation at $4640 \times g$ and were resuspended in 45 ml of ice-cold lysis buffer (Tris-HCl 0.05 M pH 8.0, EDTA 0.005 M, DTT 0.01 M). Cells were lysed by addition of Triton X100 0.2% (v/v). The cell suspension was cycled three-times between warming to 22–24°C and cooling on ice to facilitate complete lysis. The lysate was heated to 22–24°C, and at a final concentration of 7.5 mM and $MgSO_4$ DNase I (20 μg/ml) were added. Cell debris was removed by centrifugation $15300 \times g$.

Capsid particles were precipitated by adding NaCl 0.5 M and PEG 8000 6% (w/w) and stirring on ice for 1 h. The precipitate was resuspended by adding buffer G-DTT (Tris-HCl 0.02 M pH 7.5, NaCl 0.1 M, DTT 0.01 M) and pelleted by ultracentrifugation in a Beckman's Ti50.2 at 35K rpm for 2 h at 4°C. The pellet was resuspended overnight in G-DTT buffer. Particles were further purified over a 10–30% glycerol gradient by ultracentrifugation in an SW28 rotor at 27K rpm, for 1.5 h at 4°C, and the fraction was removed by a 18-gauge needle and syringe. The particles were loaded onto an anion-exchange column (Poros PI®, Applied Biosystems, Foster City, CA, USA) for complete purification. Eluted particles were buffer exchanged by two cycles of ultracentrifugation and stored in sodium phosphate buffer 0.02 M pH 7.0 containing NaCl 0.04 M and TCEP 0.002 M.

In vitro maturation

The particles were matured by acidification in sodium citrate 0.1 M, pH 4.0, NaCl 0.2 M for 5 h at room temperature, followed by ultracentrifugation and neutralization in sodium phosphate 0.02 M, pH 7.0, NaCl 0.04 M overnight. The matured particles were evaluated by SDS-PAGE or native agarose gels as described below.

Thiol-fluorophore conjugations to addressable cysteines

Particles (1 mg/ml) were reacted with a tenfold molar excess of fluorescein-5-maleimide (Invitrogen, Carlsbad, CA, USA) per coat-protein unit. The mixture was incubated for approximately 12 h at 4°C. Excess dyes were removed by anion-exchange chromatography followed by ultracentrifugation as described above. Labeling efficiencies were measured by UV/visible spectroscopy. The specific extinction coefficient of the fluorophore is 83000 $M^{-1}cm^{-1}$ at a wavelength of 492 nm. The specific extinction coefficient of the particles is 32555 $M^{-1}cm^{-1}$ at a wavelength of 280 nm.

Transferrin conjugation to C164 & C385

KMUH (*N*-[k-maleimidoundecanoic acid]hydrazide) (Pierce Biosciences (22111), Rockford, IL, USA) was conjugated to the particles through the maleimide functional group. C164 and C385 were used at a concentration of approximately 1 mg/ml in sodium phosphate 0.1 M, pH 7.0, NaCl 0.15 M, TCEP 0.0025 M to react with a tenfold molar excess linker (4 mg/ml in DMSO 10% v/v) for 1 h at room temperature followed by 4 h on ice. The reaction was dialyzed overnight against sodium phosphate 0.1 M, pH 7.0, NaCl 0.15 M to remove excess KMUH, TCEP and DMSO.

Human holotransferrin (Sigma T4132, MW ~80 kDa) was prepared by mild oxidation in sodium periodate 0.01 M in sodium acetate 0.1 M, pH 5.5, for 30 min on ice in the absence of light. The buffer was exchanged to sodium phosphate 0.1 M, pH 7.0, NaCl 0.15 M by 30 K cut-off Amicon filters (Millipore Billerica, MA, USA).

A fivefold molar excess of oxidized transferrin (Tf) was attached to the linker-activated particles by incubation for 12 h at 4°C. Tf-labeled particles were purified from nonreacted Tf using size-exclusion chromatography (SEC; as described below). Tf-labeled particles (>13 MDa) were concentrated using 100 K cut-off Amicon filters (Millipore Billerica, IL, USA).

Lysine addressability of C385-O488 & C385-Tf-O488 conjugates

To test the addressability and reactivity of solvent-exposed Lys residues on the exterior surface of C385, VNPs were incubated with Oregon Green 488 carboxylic acid, succinimidyl ester *6 isomer* (O488 NHS; Invitrogen, Carlsbad, CA, USA). O488 NHS was added to C385 in increasing molar ratios; giving a molar excess O488 NHS:C385 particle of 100:1, 200:1, 500:1, 1,000:1, 5000:1 and 10,000:1. The capsid of HK97 consists of 420 copies of identical coat protein units. X-ray structural data indicated there were four solvent-exposed Lys side chains per unit; the VNPs thus display a maximum of 1680 potentially addressable Lys residues on their exterior solvent-exposed surface. O488 NHS was dissolved in DMSO and added to C385 particles in potassium phosphate buffer 0.1 M pH 7.0. After 2 h of incubation on an overhead shaker at room temperature the reaction mixture was purified using 10 K cut-off centrifugal devices (Millipore, CA, USA), the filters were washed several times until the dye was no longer detectable in the flow-through. The concentration of recovered VNPs was determined using a Modified Lowry Assay (Thermo Fisher Scientific, IL, USA). The amount of dye per VNP was determined using UV/visible spectroscopy (Beckman Coulter, DU 800 Spectrophotometer) and the O488-specific extinction coefficient of 70,000 $M^{-1}cm^{-1}$ at a wavelength of 496 nm. For confocal

microscopy studies, C385 and C385-Tf formulations displaying approximately 600 O488 labels were used. The particles were analyzed by UV/visible spectroscopy (as described above), SEC, and native and denaturing gel electrophoresis (see later).

Size exclusion chromatography

All labeled particles were purified on a Superdex 200 column and then analyzed on a Superose6 column using the ÄKTA Explorer. Concentrated samples (500 μl of 0.2 mg/ml) were analyzed at a flow rate of 0.5 mg/ml, using sodium phosphate 0.02 M, pH 7.0, NaCl 0.04 M for preparative and phosphate buffer 0.1 M pH 7.0 for analytical column chromatography, respectively.

Gel electrophoresis

Chemically modified C385-O488 and C385-Tf-O488 VNPs were analyzed on native and denaturing gels. A total of 20 μg of sample (in loading dye, MBI Fermentas, Burlington, Canada) was analyzed on agarose gel 1.2% (w/v) in $1 \times$ TBE buffer, the running buffer was $0.5 \times$ TBE ($5 \times$ TBE = 53 g of Tris base, 27.5 g of boric acid, 20 ml of EDTA 0.5 M pH 8.0 in 1 l of MilliQ deionised water). Protein subunits were analyzed on denaturing 4–12% NuPage gels (Invitrogen) using $1 \times$ MOPS buffer (Invitrogen). A total of 20 μg sample (added LDS loading buffer; Invitrogen) was analyzed. After completion of the electrophoretic separation the particles and protein subunits, respectively, were visualized under UV light or stained using Coomassie Blue. Photographs of the gels and the densitometry measurements were prepared using the FluorChemSP imaging system.

Transmission electron microscopy

The particles at 0.02 mg/ml were absorbed on glow-discharged copper grids coated with carbon film (Electron Microscopy Sciences, Cat #CF300-Cu) for 2 min. The grids were subsequently washed twice with filtered distilled water and negatively stained with phospho-tungstic acid 2% for 45 s and air-dried completely. Specimens were imaged at a magnification of $80,000 \times$ at 2 μm defocus, using a FEI Tecnai F20 Twin transmission electron microscope at an accelerating voltage of 120 kV. Images were recorded with a Gatan Ultrascan 4k $\times$ 4k CCD camera.

Dynamic light scattering

A DynaPro Plate Reader and Dynamics software (Wyatt, CA, USA) were used for dynamic light scattering (DLS) studies. C385 and C385-Tf (0.1 mg/ml in phosphate buffered saline [PBS]) were filtered through 0.2-micron filters (Millipore) prior to analysis. Five independent measurements each were performed; each single measurement presents an average of ten acquisitions. Data were acquired at an intensity of approximately 2,000,000 counts per second at a temperature of 25°C. Statistical analysis of differences between C385 and C385-Tf was performed using Student two-tailed T-test (Microsoft Excel).

Cell lines

HeLa and HT-29 cells were obtained from ATCC (Manassas, VA, USA). Growth media and tissue culture reagents were purchased from Invitrogen. HeLa cells were grown in MEM with fetal bovine serum (FBS) 10%, L-glutamine 1% and penicillin–streptomycin 1%. HT-29 cells were grown in RPMI with FBS 10%, L-glutamine 1%, and penicillin–streptomycin 1%. Cells were incubated at 37° C and 5% CO_2.

Cellular uptake of fluorescein-labeled transferrin by tumor cells

Cells were collected using enzyme-free Hank's based cell dissociation buffer (Gibco/Invitrogen, CA, USA) and distributed in 200-μl portions at a concentration of 5×10^6 cells

ml in 96-well V-bottom shaped plates. A total of 1 μg or 10 μg of fluorescein-labeled transferrin (Tf-F) in $1 \times$ PBS pH 7.2 (Sigma, MO, USA) was added to cells and incubated at 37° C and 5% CO_2 for 4 h. Cells were washed using FACS buffer (PBS pH 7.4 containing EDTA 1 mM pH 8.0, HEPES 25 mM pH 7.5 and FBS 1%) and fixed with formaldehyde 2% e for 10 min at room temperature. Cells were resuspended and analyzed using a FACS Calibur instrument (BD Biosciences, NJ, USA). At least 10,000 events gated for single and live cells were collected. Experiments were repeated at least twice and triplets of each sample were measured and data were analyzed using FlowJo 8.6.3 software (Tree Star, Inc., Ashland, OR, USA).

Measuring interaction of C385-Tf and C164-Tf with tumor cell lines by flow cytometry

Cells were collected using enzyme-free Hank's based cell dissociation buffer (Gibco/Invitrogen) and distributed in 200 μl portions at a concentration of 5×10^6 cells/ml in 96-well V-bottom shaped plates. C385-Tf, C835, C164-Tf, or C164 were added to live cells in growth medium at a concentration of 1×10^5 particles per cell (2.2 μg or 1.7×10^{-13} mol per well). For competition binding assays, C385-Tf and C164-Tf (2.2 μg) were mixed with soluble Tf (10 μg or 1.25×10^{-10} mol) and added to live cells and incubated at 37°C and 5% CO_2. Cells were washed with FACS buffer (PBS pH 7.4 containing EDTA 1 mM pH 8.0, HEPES 25 mM pH 7.5 and FBS 1%) and subsequently fixed using formaldehyde 2% (10 min at room temperature). Prior to staining, cells were permeabilized using saponin 0.2% (Aldrich, MO, USA) in FACS buffer and staining was achieved using a polyclonal anti-HK97 antibody (1:1000 in FACS buffer + saponin 0.2%) followed by a goat anti-rabbit secondary antibody conjugated to A647 (1:2000 in FACS buffer + saponin 0.2%). All steps were carried out at 4°C. Cells were resuspended in FACS buffer and analyzed using a FACS Calibur instrument (BD Biosciences, NJ, USA). At least 10,000 events gated for single and live cells were collected. Experiments were repeated at least twice and triplets of each sample were measured and data were analyzed using FlowJo 8.6.3 software (Tree Star, Inc.).

Evaluating cell interactions with C385-O488, C385-Tf-O488, & Tf-F by fluorescence confocal microscopy

HeLa cells (5×10^4) were grown in 35-mm glass-bottom Petri dishes (Matek, MA, USA) overnight at 37°C and 5% CO_2. To test for cell interactions, 22 μg of C385-O488 (1.7×10^{-12} mol of C385), 22 μg C385-Tf-O488 particles, or 10 μg of soluble Tf-F (1.25×10^{-10} mol of Tf) were added to cells. VNPs displaying approximately 600 O488 per particles were utilized. For Tf competition, C385-Tf-O488 particles (22 μg) were mixed with soluble Tf (10 μg) and added to cells. Cells in growth media were incubated at 37°C and 5% CO_2 for 4 h. Slides were washed three-times with PBS to remove excess VNPs or Tf prior to fixing using paraformaldehyde 3%, glutaraldehyde 0.3%, $MgCl_2$ 1 mM in PBS pH 7.2 for 10 min at room temperature. Cell nuclei were stained by adding 4′,6-diamidino-2-phenylindole (DAPI; Invitrogen) (1:9500 dilution of a 1 mg/ml stock solution, for 20 min at room temperature). Slides were mounted using Vecta Shield mounting medium (Vector Laboratories). Slides were imaged using a Biorad 2100 confocal microscope with a 60× oil objective lense. Data were analyzed and images were created using ImageJ software (US NIH).

Evaluating co-localization of C385-Tf-O488 with endolysosomes by confocal microscopy

HeLa cells were collected using enzyme-free Hank's based cell dissociation buffer (Gibco/Invitrogen) and distributed in 200-μl portions at a concentration of 5×10^6 cells/ml in 96-well V-bottom shaped plates. C385-O488 or C385-Tf-O488 (2.2 μg or 1.7×10^{-13} mol of C385) was added to cells in medium and incubated for 60 min at 37°C and 5% CO_2. Cells were washed three-times with PBS to remove excess VNPs. Cells in medium were plated on 35 mm glass bottom Petri dishes (Matek) and incubated for further 3 h. Cells were washed

with PBS and fixed using paraformaldehyde 4% and glutaraldehyde 0.3% in PBS pH 7.2 for 5 min at room temperature. Cells were blocked using goat serum 5% (v/v) in PBS for 60 min at room temperature. Staining of the cell membranes was achieved by adding A555-labeled wheat germ agglutinin (WGA-A555; Invitrogen) at a dilution of 1:200 in PBS containing goat serum 1% (v/v) and incubation for 60 min at room temperature. Endolysosomes were stained using a purified antihuman CD107a (Lamp-1) antibody (BioLegend) at room temperature using a 1:500 dilution in PBS containing goat serum 1% (v/v). An A647-labeled antimouse secondary antibody was used at a 1:500 dilution in PBS containing goat serum 1% (v/v) (incubation was 60 min at room temperature for each antibody). Cells were washed and nuclei stained with DAPI (as described above). Slides were mounted, imaged, and data analyzed as described previously.

Results & discussion

Addition of reactive thiols to the surface of the HK97 VNPs

The P-II and H-II atomic structures [25,26] provided a 3D framework for genetic modification and chemical bioconjugation. Metastable P-II particles were chosen for study because the structures suggested that residues for conjugation would be more accessible compared with those in H-II and the P-II particles could, in principal, be matured after conjugation. HK97 particles have solvent-exposed lysine side chains but not cysteine residues, therefore solvent-accessible surface residues were identified for cysteine replacement. Residue 164 in P-II, located on the E-loop near icosahedral and quasi threefold axes, and residue 385, located at the C-terminus positioned near the fivefold and quasi-sixfold axes, were chosen for cysteine replacement due to their excellent accessibility and distinct surface patterns (Figure 1 & Supplementary Figure 1). Both mutant subunits expressed and assembled in *E. coli* and, based on the insertion site, were denoted C164 and C385. The particles were purified under reducing conditions with yields of approximately 120 mg/l cell culture, comparable to yields obtained expressing wild-type subunits. C164 and C385 behaved similar to wild-type when analyzed by SEC, native agarose gels, and transmission electron microscope.

Fluorescent dye conjugation

C164 and C385 each contain 420 cysteines on the surface. To address the reactivity of the cysteines, fluorescent dye-labeling was employed using maleimide-activated fluorescein. Particles were purified from excess dye by anion exchange chromatography followed by ultracentrifugation. The particle formulations were structurally stable as confirmed by SEC. UV/visible spectroscopy was employed to quantitatively determine labeling efficiency. Both mutants had labeling densities close to 30%, equal to approximately 130 dyes/particle. The extinction coefficient of the fluorescent dye on the VLP surface may not be equivalent to the extinction coefficient of free dye, therefore the labeling density estimated from UV/visible spectroscopy may be underestimated.

VNPs with surface reactive cysteines are prone to aggregate via interparticle disulfide bonds [27,28]. Therefore, we employed reducing agents such as DTT or TCEP to inhibit formation of disulfide linkages during particle purification and storage. Interestingly, the C385 formulation remained in solution and did not form any detectable aggregation during several weeks of storage. However, the C164 formulation was more prone to aggregation as indicated by native gel electrophoresis. Although the individual cysteine residues appear to be similarly reactive, their locations result in a different propensity to aggregate in solution due to interparticle disulfide linkage. According to the crystal structure of P-II, the E-loops have much a larger degree of flexibility while the C-terminus residues remain closely

associated with the capsid. Therefore, the thiols on the E-loops are expected to be more accessible to form interparticle disulfide linkages, causing aggregation of the C164 mutant.

In addition to the introduced reactive cysteines, P-II also possesses ten lysines per protein subunit, and these lysines were utilized for generating dual-functionalized particles. The atomic coordinates suggested that four lysines per subunit would be solvent-accessible. Lysines were conjugated using a *N*-hydroxysuccinimide-activated Oregon Green 488 (O488) dye. A maximum labeling of approximately 890 dyes per particle was achieved, corresponding to 50% of the 1680 accessible lysines (Supplementary Figure 3). Together, these results show that both cysteine and lysine residues are reactive and suitable for bioconjugation. Furthermore, the labeled P-II particles could be further matured *in vitro* to H-II, indicating that fluorescent dyes conjugated to either the E-loops or C-terminus did not interfere with particle maturation.

Engineering Tf & fluorescent dye dual-labeled particles

The bioconjugation chemistries described above allowed the design of receptor-targeted HK97 formulations. To test whether engineered HK97 VNPs could specifically enter into tumor cells, we employed the well-characterized Tf pathway for receptor-specific targeting. Tf is an iron-binding plasma protein whose function is to transport iron into cells and tissues. At the cell surface, iron-loaded Tf binds to its receptor (TfR), which leads to internalization of the complex via clathrin-mediated endocytosis and release of iron within the cells [29]. Rapidly dividing cells, especially those that have undergone malignant transformation have higher requirements for iron and thus over-express TfRs [30–32]. Tf-based targeting strategies are thus a popular method to effectively deliver molecules into tumor cells [29,30,33–35].

Bioconjugation strategies for chemically linking Tf to other proteins have been developed [36]. Tf is a glycosylated protein [37,38] and the carbohydrates present a versatile target for bioconjugation [39]. Multiple copies of Tf were attached to either C164 or C385 P-II with a bivalent linker that displays a maleimide functional group and a hydra-zide separated by a 20-Å hydrocarbon chain. The maleimide group is reactive toward the cysteine side chains presented on the VNPs and the hydrazide is reactive toward aldehyde groups, which were produced by mild oxidation of the carbohydrates on Tf. The reaction scheme is outlined in Figure 2. The linker was first attached to the C164 or C385 particles. Next, carbohydrates on the glycosylated Tf were oxidized to aldehydes. The oxidized Tf was then conjugated to the linker displayed on the particles (details are given in the Materials and methods section).

Dual-functionalized VLPs were also made. First, Tf was conjugated to C385 and C164, and the dye O488 was subsequently attached to surface lysines using *N*-hydroxysuccinimide activated esters (Figure 2). Characterization con-firmed that there was no interference between these attachments, the labels were covalently attached, and the particles remained structurally sound (Supplementary Figure 3). The conjugation reactions required neither harmful chemical nor did they produce hazardous byproducts, representing an environmentally friendly synthesis for targeted bioactive nanoparticle preparations. Dual-modified dye-labeled and Tf-labeled particles behaved similarly to their single-labeled counterparts (Supplementary Figure 3).

Biochemical & biophysical characterizations of the HK97-Tf particles

A combination of techniques was used to analyze the Tf-conjugated particles. SDS-PAGE and densitometry measurements were used to determine labeling efficiencies (Figure 3). Tf was conjugated to other VNPs, including CPMV and MS2 previously [40,41]; however, quantitation of the number of Tf proteins attached to these display platforms was not

reported. Based on the size of Tf and the surface area of the VNP, the theoretical maximum occupancy would be 40 Tf molecules per 30-nm-sized (T = 3) VNP, compared with 132 for HK97. We found that C385-Tf and C164-Tf displayed 101 ± 13 (or $24 \pm 3\%$ of available cysteines) and 110 ± 17 (or $26 \pm 4\%$ of available cysteines) Tf proteins per VLP, respectively. Labeling efficiencies were comparable to the coverage achieved by attaching small organic fluorophores (see above). Since the maximum possible labeling density was calculated to be 132 Tf proteins per HK97 particle, which equates to 31% of available cysteines, our observed data (~26%) indicate that Tf occupancy close to the theoretical maximum was achieved.

The SEC, DLS and transmission electron microscopy (TEM) measurements showed an increase in size for both Tf-conjugated formulations, thus confirming successful labeling with Tf. The SEC elution profile comparing Tf-labeled VNPs with native VNPs showed a change in elution volume from 7.9 to 7.8 ml upon Tf attachment. Quantitatively, the particle size increases from 27 nm in radius to 37.8 nm by DLS measurements (Figure 3). Furthermore, the Tf-labeled particles display visible additional densities on the outer surface of the particles, which can be attributed to Tf, in negative stained TEM. The increase in radius for both labeled particles was determined to be from 27 to 33 nm by a structure display program, Chimera [42]. The greater radius increase observed by DLS compared with TEM measurements is possibly due to moderate mobility of labeled Tf; thus its density is not fully visible in TEM. The greater radius in DLS could also be explained by the fact that DLS is measuring hydrated structures. Nevertheless, the data are in good agreement and with the theoretical size increase, calculated based on the dimension of Tf. An increase of approximately 10 nm in radius is expected if full coverage is accomplished, considering the diameter of Tf is approximately 10 nm including the 2-nm linker. In summary, SEC, DLS, and TEM confirmed the structural integrity and size, which is evident of successful Tf attachment.

Similar to C385 and C164, the C385-Tf and C164-Tf formulations also behaved differently in solution. As previously noted, the C164 particles were more prone to form aggregates by disulfide bonds compared with the C385 formulation. Particle aggregation was also observed with C164-Tf formulation, even though 30% of the available cysteines were covalently conjugated to Tf. The crystal structure of HK97 Prohead II suggests that C164 on the E-loop is more mobile and exposed than C385 at the C-terminus; thus the remaining cysteines are likely to be more sufficiently exposed to allow interparticle disulfide linkages. The C385 formulation is more stable and most likely suitable for future biological studies. Future studies will evaluate both labeled and nonlabeled C164 and C385 formulations *in vivo*.

Native HK97 VNPs were inert to tumor cells

Prior to exploring the cell-targeting specificity with HK97-Tf, we tested the interactions of wild-type HK97 particles with mammalian cell lines. HeLa cells, a human cervical cancer cell line, and BalbC17, a mouse fibroblast cell line, were chosen for our initial cell studies and cellular association was measured by flow cytometry. We found that, in stark contrast to other VNPs, HK97-based VNPs did not interact with cells; negligible background interactions were only observed when particles were added in high particle:cell ratio, (i.e., 10^6 particles per cell and 24 h incubation). The natural interaction of HK97 VNPs with human cells is significantly lower than other VNPs such as CPMV [43–46], the phage Qβ [47], and the rod-shaped plant virus *Potato virus X* (PVX) [48]. The latter particles naturally bind to and internalize into cells at significant levels when using 10^5 particles per cell and incubation for only 1 h. The striking differences in cell binding and uptake properties of HK97 VNPs could be explained by differences in surface charge. P-II particles have a strongly negative surface charge, with −960 e per P-II particle. CPMV also has a net

negative charge; however, it is only −180 e per particle, and is also known to interact specifically with mammalian cell surface proteins [44]. By contrast, Qβ has a positive charge of +180 e. The surface charge of PVX is not known due to the lack of a high-resolution structure. The negatively charged surface of the HK97 capsid may prevent natural interactions with the negatively charged cell membranes. The fact that HK97 particles are naturally inert to cell attachment is an excellent foundation for further development of cell-specific targeted particles.

For the further development of HK97 for tumor targeting and therapeutic applications it will be necessary to evaluate the *in vivo* properties of the particles. It is difficult to predict the performance of these particles *in vivo*. However, with regard to the surface charge, data suggest that negatively charged particles have short plasma circulation times. For example, CPMV and CCMV particles, which have a negative surface charge, have short circulation times (half-life <15 min [16,49]), whereas Qβ particles, which have a positive surface charge, have a half-life more than 3 h [50]. Whether longer or shorter circulation times are beneficial for tumor targeting in therapy has yet to be evaluated for HK97. In general, longer circulation times allow greater specificity in the target tissue; however, more rapid clearance might be desired to reduce toxic side effects [51].

Uptake of the HK97-Tf by HeLa & HT-29 cells

In vitro targeting experiments with HeLa (human cervical epithelial carcinoma) and HT-29 (human colon adenocarcinoma) cell lines were performed with HK97-Tf VNPs. Normal, nondividing cells display few to negligible numbers of TfR on their cell surface, whereas tumor cells such as HeLa and HT-29 are reported to express 10^5 or more TfR per cell [30–32]. To confirm high expression levels of TfR and uptake of Tf in these cell lines, cells were probed with Tf-F. Flow cytometry measurements confirmed both cell lines to be TfR positive, and HeLa cells showed higher expression levels compared with HT-29 cells (Supplementary Figure 4). Next, we studied the ability of tumor cell targeting using C385-Tf and C164-Tf formulations; this was assayed by flow cytometry and visualized by confocal microscopy. Uptake of C385-Tf and C164-Tf formulations by these tumor cells were confirmed (Figures 4 & 5).

To further confirm that the interaction between the Tf-labeled particles and cancer cells was mediated by the Tf-TfR pathway, the ability of soluble Tf to compete for binding with the particles was evaluated by flow cytometry and confocal microscopy. In all cases, Tf effectively competed with the conjugated particle formulations, thus confirming target specificity (Figure 4 & Supplementary Figures 1–4).

Although both particle formulations were similarly internalized into HeLa cells, high levels of uptake in HT-29 cells could only be achieved using the C385-Tf formulation. The binding efficiency of the C385-Tf formulation was threefold higher compared with C164-Tf formulation (Figure 4B). Although we almost maximized theoretical spatial occupancy, free thiols are still available on the particle surface (~300 free thiols/particle). Free thiols are highly reactive and can lead to the formation of particle aggregates via the formation of disufilde linkages, which we have indeed observed for the C164-Tf formulation. Such particle aggregate complexes (three or more particles) are probably too bulky to be efficiently internalized via clathrin-coated pits (Tf-R is internalized via clathrin-mediated endocytosis [29]). The lower uptake of C164-Tf particles in HT-29 cells may be explained by a combination of low efficiency uptake based on the formation of aggregates and low receptor expression. The fact that this effect is not observed in HeLa cells may be due to the fact that this cell line shows significantly higher expression levels of Tf-R (Supplmentary Figure 4).

Intracellular localization of HK-Tf-O488 visualized by confocal microscopy

To gain further insights into the intracellular localization and fate of the dual-labeled targeted VNPs, a series of confocal microscopy images were recorded using C385-Tf-O488 particles and HeLa cells (Figure 5). Following binding to TfR, Tf is internalized via endocytosis in clathrin-coated pits. The endocytic vesicles are then targeted to the endolysosomes, where iron is released into the cytoplasm [29,52]. To further differentiate between particles that are bound to the cell surface, versus those that are endocytosed into the cells, the cell-surface was stained using Alexa Fluor 555-labeled wheat germ agglutinin (WGA-A555), which stains the glycocalyx [53]. Cell-surface staining verified that the dual-labeled particles were indeed internalized and accumulated near the nucleus (Figure 5). Furthermore, when endolysosomes were stained using a monoclonal antibody against lysosomal-associated membrane protein 1 (Lamp1), co-localization of the C385-Tf-O488 with endolysosomes was observed, further confirming particle internalization. Interestingly, intracellular co-localization has also been observed between late endosomes and CPMV particles, although those particles are not thought to use the Tf-mediated pathway [14]. Thus it will be interesting to determine how individual targeting and internalization strategies for VNPs govern intracellular trafficking and localization in early and late endosomes.

Conclusion

This study demonstrated that, unlike other VNPs we have tested [14,44,45,47,48], unmodified HK97 PII particles have a remarkably low propensity to interact with tumor cells and are thus an attractive platform for subsequent targeting strategies. Particles specifically designed for cell targeting applications were prepared by a combination of genetic and chemical modification. Based on the atomic structure of HK97, solvent-accessible residues were identified as target sites for introduction of thiol-functional groups. The two mutant particles, C164 and C385, were evaluated and found to behave differently in reactivity, stability, and cellular interactions. We successfully targeted HK97-based nanoparticles to cancer cells *in vitro* by covalently attaching Tf onto the surface of VNPs to virtually maximum occupancy. Confocal imaging of dual-labeled formulations confirmed cellular uptake and showed that the particle formulations were internalized and localized to the endolysosomal compartment.

Targeting the Tf-R has been a popular strategy in order to direct small imaging molecules or therapeutic molecules toward tumors *in vivo* [54–57]. For example, ultrasmall, superparamagnetic iron oxide nanoparticles covalently decorated with Tf allowed *in vivo* tumor imaging in a preclinical rat model [54]. Tf-R targeting was also exploited in therapeutic applications: Tf-R targeted suicide gene-delivery and facilitated dissemination of tumors in a tumor mouse model [56]. Finally, it has been demonstrated that administration of anti-Tf-R antibodies has therapeutic effects, as the antibodies significantly inhibited proliferation of tumor cells [55,57]. It will be interesting to test whether the Tf-directed HK97 formulation itself also induces inhibitory effects on tumor growth and disease progression.

These studies demonstrate the feasibility of engineering HK97-based nanoparticles for specific cell targeting. When compared with smaller icosahedral VNPs, HK97 particles offer more available attachment sites, a larger surface area, relatively higher stability and a larger container volume for packaging therapeutic molecules, which is currently under development. Future studies will include evaluation of the *in vivo* properties of these materials. HK97 nanoparticles can be isolated at four different maturation states, providing the flexibility to use each as a unique platform for the development of the next-generation biomedical devices. Hence the HK97 platform has high potential for the development of dual-or multi-functionalized particles combining targeting, imaging and therapy.

Supplementary Material

Refer to Web version on PubMed Central for supplementary material.

Bibliography

Papers of special note have been highlighted as:

▪ of interest

▪▪ of considerable interest

1. Hajitou A, Pasqualini R, Arap W. Vascular targeting: recent advances and therapeutic perspectives. Trends cardiovasc Med. 2006; 16(3):80–88. [PubMed: 16546688]

2. Heath, Davis ME. Nanotechnology and cancer. Annu Rev Med. 2008; 59:251–265. [PubMed: 17937588]

3. Majoros IJ, Williams CR, Baker. Current dendrimer applications in cancer diagnosis and therapy. Curr Top Med Chem. 2008; 8(14):1165–1179. [PubMed: 18855703]

4. Manchester M, Singh P. Virus-based nanoparticles (VNPS): platform technologies for diagnostic imaging. Adv Drug Deliv Rev. 2006; 58(14):1505–1522. [PubMed: 17118484]

5. Soussan E, Cassel S, Blanzat M, Rico-Lattes I. Drug delivery by soft matter: matrix and vesicular carriers. Angew Chem Int Ed Engl. 2009; 48(2):274–288. [PubMed: 19072808]

6. Xing Y, Rao J. Quantum dot bioconjugates for *in vitro* diagnostics & *in vivo* imaging. Cancer Biomark. 2008; 4(6):307–319. [PubMed: 19126959]

7. Rae C, Koudelka KJ, Destito G, Estrada MN, Gonzalez MJ, Manchester M. Chemical addressability of ultraviolet-inactivated viral nanoparticles (VNPS). PLoS One. 2008; 3(10):e3315. [PubMed: 18830402]

8. Fischlechner M, Donath E. Viruses as building blocks for materials and devices. Angew Chem Int Ed Engl. 2007; 46(18):3184–3193. [PubMed: 17348058]

9. Choi VW, Mccarty DM, Samulski RJ. AAV hybrid serotypes: improved vectors for gene delivery. Curr Gene Ther. 2005; 5(3):299–310. [PubMed: 15975007]

10. Cockrell AS, Kafri T. Gene delivery by lentivirus vectors. Mol Biotechnol. 2007; 36(3):184–204. [PubMed: 17873406]

11. Douglas JT. Adenovirus-mediated gene delivery: an overview. Methods Mol Biol. 2004; 246:3–14. [PubMed: 14970581]

12. Liepold L, Anderson S, Willits D, et al. Viral capsids as MRI contrast agents. Magn Reson Med. 2007; 58(5):871–879. [PubMed: 17969126]

13. Brown WL, Mastico RA, Wu M, et al. RNA bacteriophage capsid-mediated drug delivery and epitope presentation. Intervirology. 2002; 45(4–6):371–380. [PubMed: 12602361]

14. Lewis JD, Destito G, Zijlstra A, et al. Viral nanoparticles as tools for intravital vascular imaging. Nat Med. 2006; 12(3):354–360. [PubMed: 16501571]

15. Ren Y, Wong SM, Lim LY. Folic acid-conjugated protein cages of a plant virus: a novel delivery platform for doxorubicin. Bioconjug Chem. 2007; 18(3):836–843. [PubMed: 17407258]

16. Singh P, Prasuhn D, Yeh RM, et al. Bio-distribution, toxicity and pathology of cowpea mosaic virus nanoparticles *in vivo*. J Control Release. 2007; 120(1–2):41–50. [PubMed: 17512998]

17. Dhillon EK, Dhillon TS, Lai AN, Linn S. Host range, immunity and antigenic properties of lambdoid coliphage hk97. J Gen Virol. 1980; 50(1):217–220. [PubMed: 6449561]

18▪. Duda RL, Hempel J, Michel H, Shabanowitz J, Hunt D, Hendrix RW. Structural transitions during bacteriophage HK97 head assembly. J Mol Biol. 1995; 247(4):618–635. Biochemical features of the HK97 virus-like particles. [PubMed: 7723019]

19. Gan L, Conway JF, Firek BA, et al. Control of crosslinking by quaternary structure changes during bacteriophage HK97 maturation. Mol Cell. 2004; 14(5):559–569. [PubMed: 15175152]

20. Ross PD, Cheng N, Conway JF, et al. Crosslinking renders bacteriophage HK97 capsid maturation irreversible and effects an essential stabilization. EMBO J. 2005; 24(7):1352–1363. [PubMed: 15775971]

21. Loo L, Guenther RH, Lommel SA, Franzen S. Encapsidation of nanoparticles by red clover necrotic mosaic virus. J Am Chem Soc. 2007; 129(36):11111–11117. [PubMed: 17705477]

22. Minten IJ, Hendriks LJ, Nolte RJ, Cornelissen JJ. Controlled encapsulation of multiple proteins in virus capsids. J Am Chem Soc. 2009; 131(49):17771–17773. [PubMed: 19995072]

23. Duda RL, Martincic K, Hendrix RW. Genetic basis of bacteriophage HK97 prohead assembly. J Mol Biol. 1995; 247(4):636–647. [PubMed: 7723020]

24. Duda RL, Martincic K, Xie Z, Hendrix RW. Bacteriophage HK97 head assembly. FEMS Microbiol Rev. 1995; 17(1–2):41–46. [PubMed: 7669350]

25▪▪. Gertsman I, Gan L, Guttman M, et al. An unexpected twist in viral capsid maturation. Nature. 2009; 458(7238):646–650. Provides the atomic resolution structure of P-II subunits suggesting the solvent accessible regions of the particles. [PubMed: 19204733]

26▪. Wikoff WR, Liljas L, Duda RL, Tsuruta H, Hendrix RW, Johnson JE. Topologically linked protein rings in the bacteriophage HK97 capsid. Science. 2000; 289(5487):2129–2133. Provides the atomic resolution structure of H-II subunits highlighting the N-arm, A-domain, P-domain and the E-loop. [PubMed: 11000116]

27▪. Steinmetz NF, Evans DJ, Lomonossoff GP. Chemical introduction of reactive thiols into a viral nanoscaffold: a method that avoids virus aggregation. Chembiochem. 2007; 8(10):1131–1136. Another example of investigating targeted cell entry with viral nanoparticles (VNPs) by flow cytometry and confocal microscopy. [PubMed: 17526061]

28▪▪. Wang Q, Lin T, Johnson JE, Finn MG. Natural supramolecular building blocks: cysteine-added mutants of cowpea mosaic virus. Chem Biol. 2002; 9(7):813–819. Another example of addition of cysteines to the surface of VNPs for bioconjugation. [PubMed: 12144925]

29▪▪. Qian ZM, Li H, Sun H, Ho K. Targeted drug delivery via the transferrin receptor-mediated endocytosis pathway. Pharmacol Rev. 2002; 54(4):561–587. Demonstrates the effectiveness of delivering drugs using transferrin (Tf) receptor-mediated pathway. [PubMed: 12429868]

30. Agarwal A, Saraf S, Asthana A, Gupta U, Gajbhiye V, Jain NK. Ligand based dendritic systems for tumor targeting. Int J Pharm. 2008; 350(1–2):3–13. [PubMed: 18162345]

31. Inoue T, Cavanaugh PG, Steck PA, Brunner N, Nicolson GL. Differences in transferrin response and numbers of transferrin receptors in rat and human mammary carcinoma lines of different metastatic potentials. J Cell Physiol. 1993; 156(1):212–217. [PubMed: 8314858]

32. Bridges KR, Smith BR. Discordance between transferrin receptor expression and susceptibility to lysis by natural killer cells. J Clin Invest. 1985; 76(3):913–918. [PubMed: 2995450]

33. Faulk WP, Hsi BL, Stevens PJ. Transferrin and transferrin receptors in carcinoma of the breast. Lancet. 1980; 2(8191):390–392. [PubMed: 6105517]

34. Gatter KC, Brown G, Trowbridge IS, Woolston RE, Mason DY. Transferrin receptors in human tissues: Their distribution and possible clinical relevance. J Clin Pathol. 1983; 36(5):539–545. [PubMed: 6302135]

35. Huebers HA, Finch CA. The physiology of transferrin and transferrin receptors. Physiol Rev. 1987; 67(2):520–582. [PubMed: 3550839]

36. Jiang YY, Liu C, Hong MH, Zhu SJ, Pei YY. Tumor cell targeting of transferrin-PEG-TNF-α conjugate via a receptor-mediated delivery system: design, synthesis, and biological evaluation. Bioconjug Chem. 2007; 18(1):41–49. [PubMed: 17226956]

37. Macgillivray RT, Mendez E, Shewale JG, Sinha SK, Lineback-Zins J, Brew K. The primary structure of human serum transferrin. The structures of seven cyanogen bromide fragments and the assembly of the complete structure. J Biol Chem. 1983; 258(6):3543–3553. [PubMed: 6833213]

38. Bewley MC, Tam BM, Grewal J, et al. X-ray crystallography and mass spectroscopy reveal that the N-lobe of human transferrin expressed in *Pichia pastoris* is folded correctly but is glycosylated on serine-32. Biochemistry. 1999; 38(8):2535–2541. [PubMed: 10029548]

39▪▪. Chamow SM, Kogan TP, Peers DH, Hastings RC, Byrn RA, Ashkenazi A. Conjugation of soluble cd4 without loss of biological activity via a novel carbohydrate-directed cross-linking

reagent. J Biol Chem. 1992; 267(22):15916–15922. Demonstrates the carbohydrated-directed chemistry that was used to conjugate Tf to the HK97 VNPs. [PubMed: 1639820]

40. Sen Gupta S, Kuzelka J, Singh P, Lewis WG, Manchester M, Finn MG. Accelerated bioorthogonal conjugation: a practical method for the ligation of diverse functional molecules to a polyvalent virus scaffold. Bioconjug Chem. 2005; 16(6):1572–1579. [PubMed: 16287257]

41. Wu M, Brown WL, Stockley PG. Cell-specific delivery of bacteriophage-encapsidated ricin a chain. Bioconjug Chem. 1995; 6(5):587–595. [PubMed: 8974458]

42. Pettersen EF, Goddard TD, Huang CC, et al. UCSF Chimera – a visualization system for exploratory research and analysis. J Comput Chem. 2004; 25(13):1605–1612. [PubMed: 15264254]

43. Gonzalez MJ, Plummer EM, Rae CS, Manchester M. Interaction of cowpea mosaic virus (CPMV) nanoparticles with antigen presenting cells *in vitro* and *in vivo*. PLoS One. 2009; 4(11):e7981. [PubMed: 19956734]

44. Koudelka KJ, Destito G, Plummer EM, Trauger SA, Siuzdak G, Manchester M. Endothelial targeting of cowpea mosaic virus (CPMV) via surface vimentin. PLoS Pathog. 2009; 5(5):e1000417. [PubMed: 19412526]

45. Shriver LP, Koudelka KJ, Manchester M. Viral nanoparticles associate with regions of inflammation and blood brain barrier disruption during CNS infection. J Neuroimmunol. 2009; 211(1–2):66–72. [PubMed: 19394707]

46. Steinmetz NF, Manchester M. Pegylated viral nanoparticles for biomedicine: the impact of PEG chain length on VNP cell interactions *in vitro* and *ex vivo*. Biomacromolecules. 2009; 10(4):784–792. [PubMed: 19281149]

47. Steinmetz NF, Hong V, Spoerke ED, et al. Buckyballs meet viral nanoparticles: Candidates for biomedicine. J Am Chem Soc. 2009; 131(47):17093–17095. [PubMed: 19904938]

48. Steinmetz NF, Mertens ME, Taurog RE, et al. Potato virus X as a novel platform for potential biomedical applications. Nano Lett. 2010; 10(1):305–312. [PubMed: 20017489]

49. Kaiser CR, Flenniken ML, Gillitzer E, et al. Biodistribution studies of protein cage nanoparticles demonstrate broad tissue distribution and rapid clearance *in vivo*. Int J Nanomedicine. 2007; 2(4):715–733. [PubMed: 18203438]

50. Prasuhn De, Singh P, Strable E, Brown S, Manchester M, Finn MG. Plasma clearance of bacteriophage qbeta particles as a function of surface charge. J Am Chem Soc. 2008; 130(4):1328–1334. [PubMed: 18177041]

51. Thurber GM, Schmidt MM, Wittrup KD. Antibody tumor penetration: transport opposed by systemic and antigen-mediated clearance. Adv Drug Deliv Rev. 2008; 60:1421–1434. [PubMed: 18541331]

52. Li H, Qian ZM. Transferrin/transferrin receptor-mediated drug delivery. Med Res Rev. 2002; 22(3):225–250. [PubMed: 11933019]

53. Wright CS. Structural comparison of the two distinct sugar binding sites in wheat germ agglutinin isolectin II. J Mol Biol. 1984; 178(1):91–104. [PubMed: 6548265]

54. Kresse M, Wagner S, Pfefferer D, Lawaczeck R, Elste V, Semmler W. Targeting of ultrasmall superparamagnetic iron oxide (USPIO) particles to tumor cells *in vivo* by using transferrin receptor pathways. Magn Reson Med. 1998; 40(2):236–242. [PubMed: 9702705]

55. Qing Y, Shuo W, Zhihua W, et al. The *in vitro* antitumor effect and *in vivo* tumor-specificity distribution of human–mouse chimeric antibody against transferrin receptor. Cancer Immunol Immunother. 2006; 55(9):1111–1121. [PubMed: 16341531]

56. Sato Y, Yamauchi N, Takahashi M, et al. *In vivo* gene delivery to tumor cells by transferrin–streptavidin–DNA conjugate. FASEB J. 2000; 14(13):2108–2118. [PubMed: 11023995]

57. White S, Taetle R, Seligman PA, Rutherford M, Trowbridge IS. Combinations of anti-transferrin receptor monoclonal antibodies inhibit human tumor cell growth *in vitro* and *in vivo*: evidence for synergistic antiproliferative effects. Cancer Res. 1990; 50(19):6295–6301. [PubMed: 2400993]
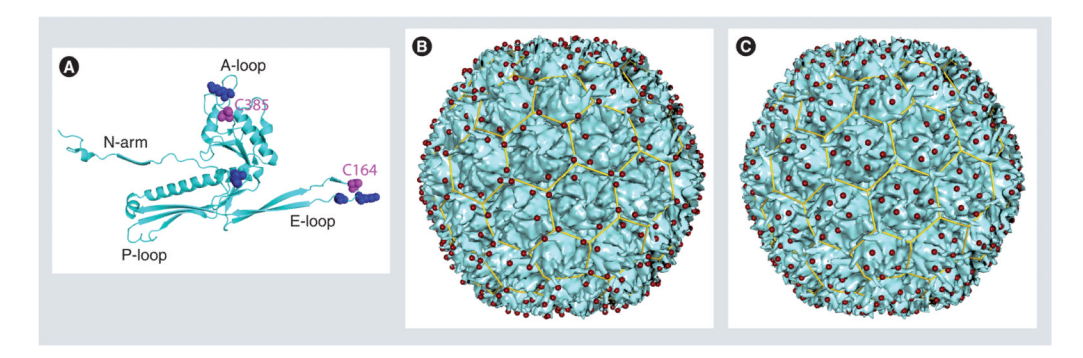
Figure 1. HK97 Prohead-II particles displaying surface reactive cysteines
(A) The capsid subunit, displaying modified cysteines (magenta) at the E-loop (C164) and the C-terminus (C385), and proposed solvent-accessible lysine residues shown in blue. **(B & C)** The P-II particle forms a T = 7 laevo icosahedral lattice, with red spheres indicating the locations of genetically introduced cysteines at residues 164 (C164; **[B]**) and 385 (C385; **[C]**).
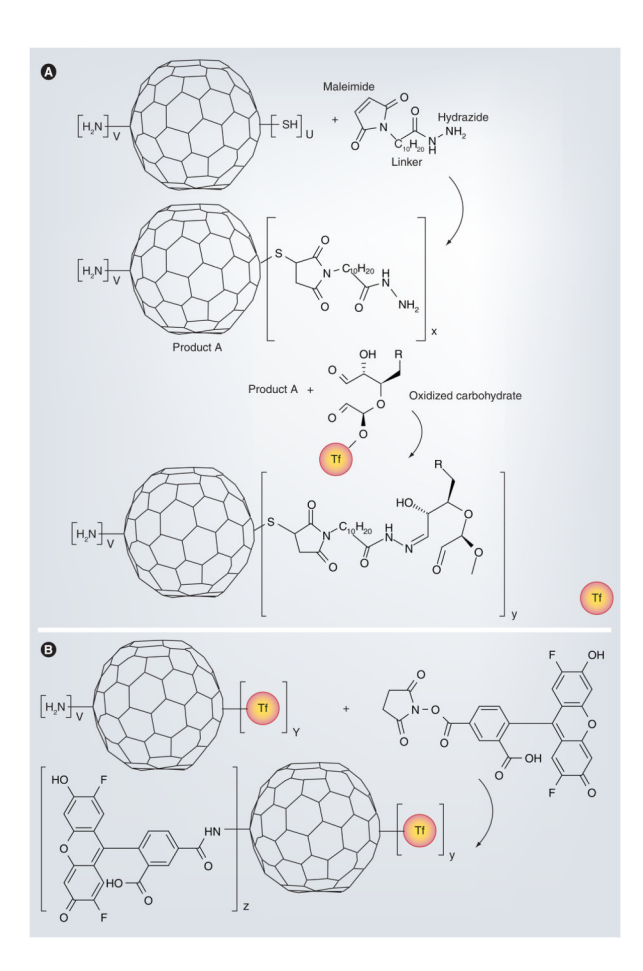
Figure 2. Reaction schemes for the preparation of transferrin-conjugated HK97 nanoparticles
(A) The particles (either C164 or C385) were reacted with the bivalent linker KMUH containing maleimide and hydrazide. The reduced cysteines on the particles react with the maleimide on the linker. Linker-activated particles react to hydrazides, forming a hydrazone linkage with oxidized carbohydrates on glycosylated human Tf to yield the final product.
(B) Secondary fluorescent labeling of the Tf-conjugated particles with Oregon Green 488 by lysine-NHS ester linkage.
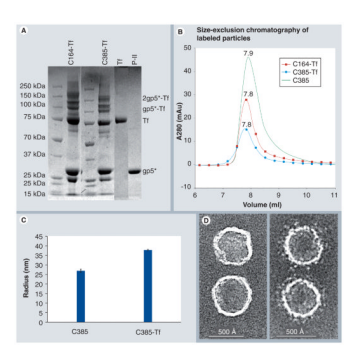KMUH: *N*-(k-maleimidoundecanoic acid)hydrazide; Tf: Transferrin.

Figure 3. Biochemical evaluation of the transferrin-conjugated particles

(A) SDS-PAGE of Tf-conjugated particles. The P-II capsid protein gp5* containing residues 104–385 shows as 31 kDa. Multimers of labeled gp5* are due to intersubunit cross-links prior to gel electrophoresis, which is a known behavior of P-II. Free transferrin ran as 76 kDa as a result of self-dimerization of a free to a conjugated Tf. **(B)** Size exclusion chromatograms of C164-Tf and C385-Tf particles compared with unconjugated particles. Tf-conjugated particles eluted earlier than unlabeled particles, indicating an increase in particle radius upon Tf conjugation. **(C)** Radius of C385 and C385-Tf as determined using dynamic light scattering. C385 has an averaged radius of 27.0 nm (polydispersity was 12.8%), and C385-Tf measures an averaged radius of 37.8 nm (polydispersity was 14%). Data were obtained from five independent measurements; each dataset is averaged from ten acquisitions. The error bars show ± standard deviation. Statistical analysis of differences between C385 and C385-Tf was performed using Student two-tailed T-test (Microsoft Excel) with $p < 5 \times 10^{-6}$. **(d)** Negative-stained electron micrographs of C385-Tf particles (right) display visible density attributed to conjugated Tf's on the exterior capsid surface compared to unlabeled C385 particles (left). Conjugated particles have a radius of approximately 33 nm compared to approximately 27 nm for C385 particles. Tf: Transferrin.
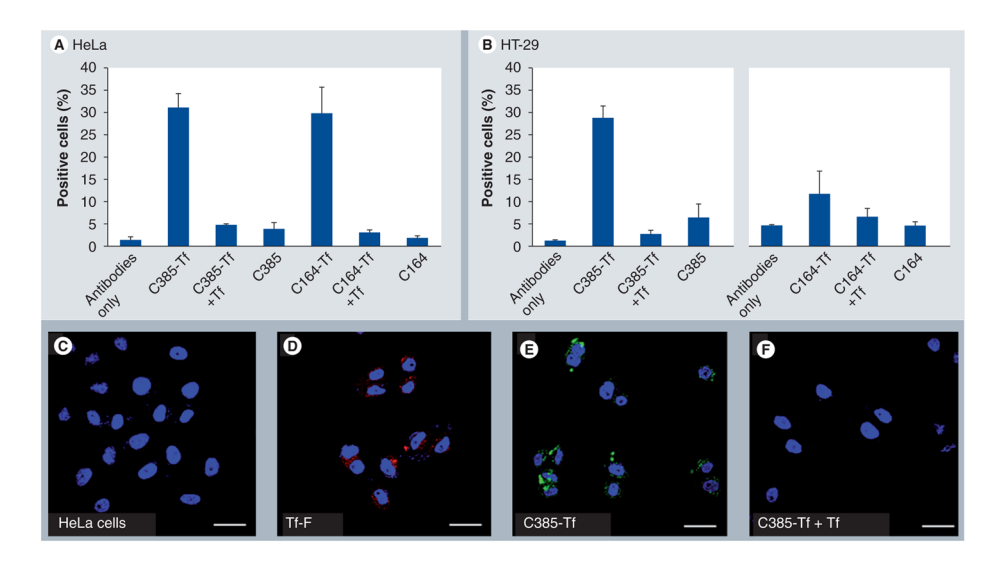
Figure 4. Targeting C385-Tf and C164-Tf to HeLa and HT-29 tumor cells *in vitro*
(A–B) Cellular interactions were analyzed by flow cytometry. The percentage of fluorescence-positive cells was analyzed in triplicate using FlowJo software. Error bars indicate mean standard deviation. **(C–F)** Uptake of C385-Tf in HeLa cells measured by confocal microscopy using fluorescent labeled Tf-F and C385-Tf-O488 and HeLa cells. **(C)** HeLa cells alone. **(d)** Tf-F uptake into HeLa cells. Tf-F is pseudocolored in red. **(e)** C385-Tf-O488 uptake into HeLa cells. For high-resolution images, see Figure 5. **(F)** Inhibition of C385-Tf-O488 uptake by competition with free Tf. Nuclei are shown in blue (DAPI), Tf-F is pseudocolored in red, C385-Tf-O488 is shown in green. The scale bar is 30 μm. Tf: Transferrin; Tf-F: Fluorescein-labeled transferrin.
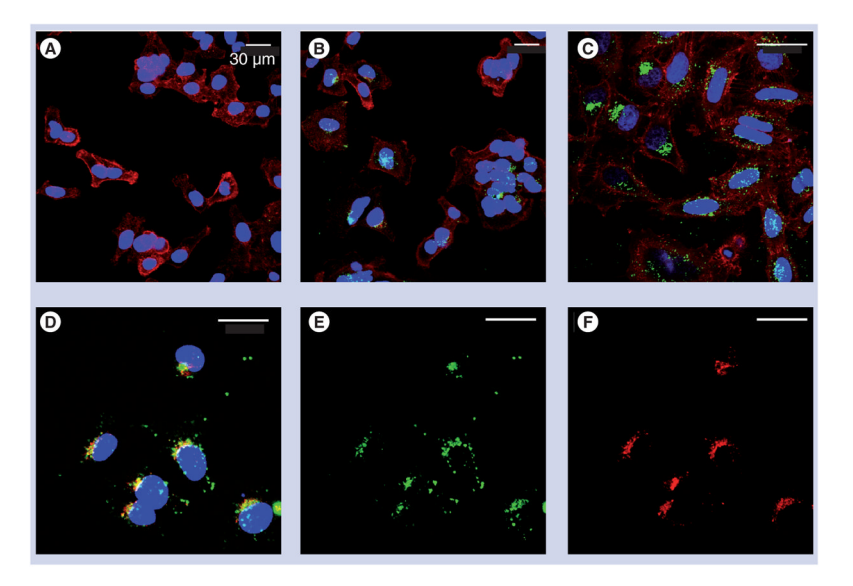
Figure 5. Intracellular localization of C385-transferrin in HeLa cells
(A) C385-O488 (green, negative control) and WGA-A555 (red, staining cell surface). **(B & C)** C385-Tf-O488 (green) and WGA-A555 (red). Nuclei are shown in blue (DAPI). **(D)** Merge: C385-Tf-O488 (green, **E**), Lamp-1 (red, **F**), nuclei (blue), yellow signal = colocalization of C385-Tf-O488 and Lamp-1 signal, **(E)** C385-Tf-O488 (green), **(F)** endolysosomes stained with Lamp-1 (red). The scale bar is 30 μm.